Using ALE-VMS to compute aerodynamic derivatives of bridge sections

Tore A. Helgedagsrud[a,*], Yuri Bazilevs[b], Artem Korobenko[c], Kjell M. Mathisen[a], Ole A. Øiseth[a]

[a]*Department of Structural Engineering, Norwegian University of Science and Technology (NTNU), Richard Birkelands v 1a, NO-7491 Trondheim, Norway*
[b]*School of Engineering, Brown University, 184 Hope Street, Providence, RI 02912, USA*
[c]*Department of Mechanical and Manufacturing Engineering, University of Calgary, 2500 Uni. Dr. NW, Calgary, Alberta Canada T2N 1N4*

Abstract

Aeroelastic analysis is a major task in the design of long-span bridges, and recent developments in computer power and technology have made Computational Fluid Dynamics (CFD) an important supplement to wind tunnel experiments. In this paper, we employ the Finite Element Method (FEM) with an effective mesh-moving algorithm to simulate the forced-vibration experiments of bridge sectional models. We have augmented the formulation with weakly-enforced essential boundary conditions, and a numerical example illustrates how weak enforcement of the no-slip boundary condition gives a very accurate representation of the aeroelastic forces in the case of relatively coarse boundary layer mesh resolution. To demonstrate the accuracy of the method for industrial applications, the complete aerodynamic derivatives for lateral, vertical and pitching degrees-of-freedom are

*Corresponding author.
Email addresses: tore.a.helgedagsrud@ntnu.no (Tore A. Helgedagsrud), jbazilevs@ucsd.edu (Yuri Bazilevs), artem.korobenko@ucalgary.ca (Artem Korobenko), kjell.mathisen@ntnu.no (Kjell M. Mathisen), ole.oiseth@ntnu.no (Ole A. Øiseth)

Preprint submitted to Computers and Fluids *April 18, 2018*

computed for two bridge deck sectional models and compared with experimental wind-tunnel results. Although some discrepancies are seen in the high range of reduced velocities, the proposed numerical framework generally reproduces the experiments with good accuracy and proves to be a beneficial tool in simulation of bluff body aerodynamics for bridge design.
Keywords: Bridge aerodynamics, Aeroelasticity, Finite Element Method, Aerodynamic derivatives, ALE-VMS

---

1. Introduction

Although the Finite Volume Method (FVM) is the most widely-used and thoroughly validated method in Computational Fluid Dynamics (CFD), the Finite Element Method (FEM) has seen huge development in efficient and accurate modeling for CFD and Fluid–Structure Interaction (FSI) problems in the recent decades. An important advantage with FEM is its natural ability to handle deforming spatial domains, making it suitable for multi-physics simulations such as FSI. Moreover, the continuous field variables makes handling of derived quantities very convenient.

The core technology used in this work is the Arbitrary Lagrangian–Eulerian Variational Multiscale (ALE-VMS) formulation of the Navier–Stokes equations for incompressible flows [1–6] with weak enforcement of essential boundary conditions (BCs) [7–12]. The former may be viewed as an extension of the residual-based variational multiscale (RBVMS) method for turbulence modeling [13–15] to moving domains using the ALE technique [16], while the latter acts as a near-wall model and relaxes the boundary-layer resolution requirements for engineering applications without significant loss of solution accuracy. VMS methods, in context of both ALE and space–time (ST) techniques, have been successfully applied to a wide range of engineering problems [4, 5, 11, 12, 17–53], including computation of aerodynamic derivatives in 2D [54].

To guarantee good mesh quality near the bridge surface during forced-vibration simulations, the Solid-Extension Mesh Moving Technique (SEMMT) was adopted [55–60]. In this approach, structured layers of elements generated around the solid object move together with solid object, undergoing a rigid-body motion, and thus preserving the original mesh quality. With this computational framework we compute the aerodynamic derivatives from 3D numerical simulations of the forced-vibration experiments and compare with corresponding wind tunnel experiments for two carefully chosen sections: A rectangular prism with aspect ratio 10, and a 1:50 scale model of the Hardanger bridge [61]. The rectangular prism, characterized by strongly detached flows at the leading edge, represents the classical example in bluff body aerodynamics and its flutter characteristics have been studied numerically using FVM and various turbulence models in, e.g., [62–64]. The Hardanger Bridge, with a more streamlined shape, represents the new generation of long-span suspension bridges with highly optimized aerodynamic design. A fully coupled free-vibration Fluid-Object Interaction (FOI) simulation of the same bridge was carried out in [65]. Numerous forced-vibration experiments of similar generic bridge sections have been performed numerically in, e.g., [66–69] including 2D FEM in [54, 70].

The simulations carried out in this paper have been designed to reproduce the experimental setup as closely as possible, and since the wind tunnel tests presented herein are performed specifically for this work, we are to a much greater extent able to compare and evaluate the results down to each time series. A description of our forced-vibration experimental setup are given in [71].

We consider an extruded slice of the bridge deck, which is treated as a rigid object. Because the deck motion is prescribed in forced-vibration, this type of problem gives a one-way dependence between the fluid mesh and fluid mechanics problem. In the fluid mesh problem the boundary layer elements, which constitute a significant portion of the nodal degrees-of-freedom, are treaded as rigid. This results in a computationally efficient solution of the fluid mesh problem while keeping the mesh distortion at a minimum.

The governing equations are presented in Sec. 2 and the discrete ALE-VMS formulation with weakly-enforced BCs is presented in Sec. 3. Sec. 4 presents aeroelastic forces in the context of bridge engineering and in Sec. 5 the analysis setup is presented. Numerical results are given in Sec. 6, and conclusions are drawn in Sec. 7.

2. Governing equations for fluid mechanics in moving domains

In this section we present the Navier-Stokes equations for incompressible flows in an ALE description. Let $\hat{\Omega} \in \mathbb{R}^{n_{sd}}$, $n_{sd} = 2, 3$, represent the reference fluid mechanics domain with coordinates $\hat{\mathbf{x}}$ and boundary $\hat{\Gamma}$, and let $\Omega_t \in \mathbb{R}^{n_{sd}}$, $n_{sd} = 2, 3$, represent the current-configuration fluid mechanics domain with coordinates $\mathbf{x}$ and boundary Γ_t. The ALE mapping is given by the time-dependent displacements of the fluid domain, $\hat{\mathbf{y}}\left(\hat{\mathbf{x}}, t\right)$:

$$\mathbf{x}(t) = \hat{\mathbf{x}} + \hat{\mathbf{y}}\left(\hat{\mathbf{x}}, t\right). \tag{1}$$

See Fig. 1. We let $\mathcal{S}_u$ and $\mathcal{S}_p$ denote the appropriate sets of infinite-dimensional trial functions for the fluid velocity $\mathbf{u}$ and pressure p, respectively, and we de-

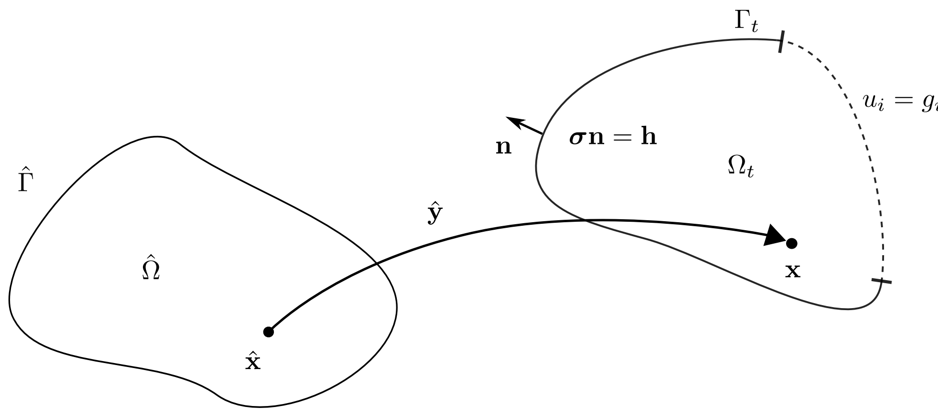

Figure 1: Fluid domain and its boundary with outward normal vector $\mathbf{n}$ in the reference and current configuration.

fine their corresponding test functions $\mathcal{V}_u$ and $\mathcal{V}_p$. The trial functions satisfy the essential boundary conditions $u_i = g_i$ on the $(\Gamma_t)_{gi}$ part of Γ_t.

The variational formulation of the fluid mechanics problem is stated in terms of the semi-linear and linear forms B and F, respectively, as follows. Find $\mathbf{u} \in \mathcal{S}_u$ and $p \in \mathcal{S}_p$, such that $\forall \mathbf{w} \in \mathcal{V}_u$ and $q \in \mathcal{V}_p$:

$$B\left(\{\mathbf{w}, q\}, \{\mathbf{u}, p\}; \hat{\mathbf{u}}\right) - F\left(\{\mathbf{w}, q\}\right) = 0, \tag{2}$$

where

$$\begin{aligned} B(\{\mathbf{w}, q\}, \{\mathbf{u}, p\}; \hat{\mathbf{u}}) = & \\ & \int_{\Omega_t} \mathbf{w} \cdot \rho \left(\left.\frac{\partial \mathbf{u}}{\partial t}\right|_{\hat{x}} + (\mathbf{u} - \hat{\mathbf{u}}) \cdot \boldsymbol{\nabla} \mathbf{u} \right) \mathrm{d}\Omega \\ & + \int_{\Omega_t} \boldsymbol{\varepsilon}(\mathbf{w}) : \boldsymbol{\sigma}(\mathbf{u}, p) \, \mathrm{d}\Omega + \int_{\Omega_t} q \boldsymbol{\nabla} \cdot \mathbf{u} \, \mathrm{d}\Omega, \end{aligned} \tag{3}$$

and

$$F\left(\{\mathbf{w}, q\}\right) = \int_{\Omega_t} \mathbf{w} \cdot \rho \mathbf{f} \, \mathrm{d}\Omega + \int_{(\Gamma_t)_h} \mathbf{w} \cdot \mathbf{h} \, \mathrm{d}\Gamma. \tag{4}$$

Here, ρ is the density, $\mathbf{f}$ the body forces, $\mathbf{h}$ the prescribed surface tractions on the $(\Gamma_t)_h$ part of Γ_t and $\hat{\mathbf{u}} = \frac{\partial \hat{\mathbf{y}}}{\partial t}\big|_{\hat{x}}$ is the fluid domain velocity. The Cauchy stress tensor $\boldsymbol{\sigma}$ is defined as:

$$\boldsymbol{\sigma}(\mathbf{u}, p) = -p\mathbf{I} + 2\mu\boldsymbol{\varepsilon}(\mathbf{u}), \tag{5}$$

where $\mathbf{I}$ is the identity tensor, μ the dynamic viscosity and $\boldsymbol{\varepsilon}(\mathbf{u})$ the symmetric strain-rate tensor of $\mathbf{u}$, given by:

$$\boldsymbol{\varepsilon}(\mathbf{u}) = \frac{1}{2}\left(\nabla\mathbf{u} + \nabla\mathbf{u}^T\right). \tag{6}$$

3. Discrete ALE-VMS formulation with weakly-enforced BCs

In the following we present the ALE-VMS formulation with weakly-enforced boundary conditions and the mesh-moving strategy for forced-vibration analyses. At the discrete level the fluid domain is partitioned into n_{el} finite element subdomains Ω_t^e, and the boundary Γ_t is decomposed into n_{eb} surface elements denoted Γ_t^b. We define the finite-dimensional functional spaces for velocity, pressure and fluid mesh displacement respectively as $\mathcal{S}_u^h$, $\mathcal{S}_p^h$ and $\mathcal{S}_m^h$, and their corresponding test functions as $\mathcal{V}_u^h$, $\mathcal{V}_p^h$ and $\mathcal{V}_m^h$. Superscript h indicates that its attribute is finite-dimensional.

The ALE-VMS formulation augmented with weakly-enforced BCs is then given: Find $\mathbf{u}^h \in \mathcal{S}_u^h$, $p^h \in \mathcal{S}_p^h$ and $\hat{\mathbf{y}}^h \in \mathcal{S}_m^h$, such that $\forall \mathbf{w}^h \in \mathcal{V}_u^h$, $q^h \in \mathcal{V}_p^h$ and $\mathbf{w}_m^h \in \mathcal{V}_m^h$:

$$
\begin{aligned}
&B^{VMS}\left(\left\{\mathbf{w}^h, q^h\right\}, \left\{\mathbf{u}^h, p^h\right\}; \hat{\mathbf{u}}^h\right)\\
&+B^{WBC}\left(\left\{\mathbf{w}^h, q^h\right\}, \left\{\mathbf{u}^h, p^h\right\}; \hat{\mathbf{u}}^h\right)\\
&-F^{VMS}\left(\left\{\mathbf{w}^h, q^h\right\}\right)\\
&+B^{MSH}\left(\left\{\mathbf{w}_m^h\right\}, \hat{\mathbf{y}}^h(t)\right) = 0,
\end{aligned} \tag{7}
$$

where

$$
\begin{aligned}
&B^{VMS}\left(\left\{\mathbf{w}^h, q^h\right\}, \left\{\mathbf{u}^h, p^h\right\}; \hat{\mathbf{u}}^h\right) = \\
&\qquad \int_{\Omega_t} \mathbf{w}^h \cdot \rho \left(\left.\frac{\partial \mathbf{u}^h}{\partial t}\right|_{\hat{x}} + \left(\mathbf{u}^h - \hat{\mathbf{u}}^h\right) \cdot \boldsymbol{\nabla} \mathbf{u}^h \right) \mathrm{d}\Omega \\
&\quad + \int_{\Omega_t} \boldsymbol{\varepsilon}(\mathbf{w}^h) : \boldsymbol{\sigma}(\mathbf{u}^h, p^h) \, \mathrm{d}\Omega + \int_{\Omega_t} q^h \boldsymbol{\nabla} \cdot \mathbf{u}^h \, \mathrm{d}\Omega \\
&\quad + \sum_{e=1}^{n_{el}} \int_{\Omega_t^e} \tau_{\mathrm{SUPS}} \left(\left(\mathbf{u}^h - \hat{\mathbf{u}}^h\right) \cdot \boldsymbol{\nabla} \mathbf{w}^h + \frac{\boldsymbol{\nabla} q^h}{\rho} \right) \cdot \\
&\qquad\qquad\qquad\qquad \mathbf{r}_M \left(\mathbf{u}^h, p^h\right) \, \mathrm{d}\Omega \\
&\quad + \sum_{e=1}^{n_{el}} \int_{\Omega_t^e} \rho \nu_{\mathrm{LSIC}} \boldsymbol{\nabla} \cdot \mathbf{w}^h \mathrm{r}_C(\mathbf{u}^h) \, \mathrm{d}\Omega \\
&\quad - \sum_{e=1}^{n_{el}} \int_{\Omega_t^e} \tau_{\mathrm{SUPS}} \mathbf{w}^h \cdot \left(\mathbf{r}_M \left(\mathbf{u}^h, p^h\right) \cdot \boldsymbol{\nabla} \mathbf{u}^h \right) \mathrm{d}\Omega \\
&\quad - \sum_{e=1}^{n_{el}} \int_{\Omega_t^e} \frac{\boldsymbol{\nabla} \mathbf{w}^h}{\rho} : \left(\tau_{\mathrm{SUPS}} \mathbf{r}_M \left(\mathbf{u}^h, p^h\right) \right) \otimes \\
&\qquad\qquad\qquad \left(\tau_{\mathrm{SUPS}} \mathbf{r}_M \left(\mathbf{u}^h, p^h\right) \right) \mathrm{d}\Omega,
\end{aligned} \tag{8}
$$

$$
F^{VMS}\left(\left\{\mathbf{w}^h, q^h\right\}\right) = \int_{\Omega_t} \mathbf{w}^h \cdot \rho \, \mathbf{f}^h \, \mathrm{d}\Omega + \int_{(\Gamma_t)_h} \mathbf{w}^h \cdot \mathbf{h}^h \, \mathrm{d}\Gamma, \tag{9}
$$

$$
\begin{aligned}
B^{WBC} & \left(\left\{\mathbf{w}^h, q^h\right\}, \left\{\mathbf{u}^h, p^h\right\}; \hat{\mathbf{u}}^h\right) = \\
& - \sum_{b=1}^{n_{eb}} \int_{\Gamma_t^b \cap (\Gamma_t)_g} \mathbf{w}^h \cdot \boldsymbol{\sigma}\left(\mathbf{u}^h, p^h\right) \mathbf{n} \, \mathrm{d}\Gamma \\
& - \sum_{b=1}^{n_{eb}} \int_{\Gamma_t^b \cap (\Gamma_t)_g} \left(2\mu \boldsymbol{\varepsilon}\left(\mathbf{w}^h\right) \mathbf{n} + q^h \mathbf{n}\right) \cdot \left(\mathbf{u}^h - \mathbf{g}^h\right) \, \mathrm{d}\Gamma \\
& - \sum_{b=1}^{n_{eb}} \int_{\Gamma_t^b \cap (\Gamma_t)_g^-} \mathbf{w}^h \cdot \rho \left(\left(\mathbf{u}^h - \hat{\mathbf{u}}^h\right) \cdot \mathbf{n}\right) \left(\mathbf{u}^h - \mathbf{g}^h\right) \, \mathrm{d}\Gamma \\
& + \sum_{b=1}^{n_{eb}} \int_{\Gamma_t^b \cap (\Gamma_t)_g} \tau_{\mathrm{TAN}}^B \left(\mathbf{w}^h - \left(\mathbf{w}^h \cdot \mathbf{n}\right) \mathbf{n}\right) \cdot \\
& \qquad \qquad \left(\left(\mathbf{u}^h - \mathbf{g}^h\right) \left(\left(\mathbf{u}^h - \mathbf{g}^h\right) \cdot \mathbf{n}\right) \mathbf{n}\right) \, \mathrm{d}\Gamma \\
& + \sum_{b=1}^{n_{eb}} \int_{\Gamma_t^b \cap (\Gamma_t)_g} \tau_{\mathrm{NOR}}^B \left(\mathbf{w}^h \cdot \mathbf{n}\right) \left(\left(\mathbf{u}^h - \mathbf{g}^h\right) \cdot \mathbf{n}\right) \, \mathrm{d}\Gamma.
\end{aligned} \tag{10}
$$

and

$$
\begin{aligned}
B^{MSH} & \left(\left\{\mathbf{w}_m^h\right\}, \hat{\mathbf{y}}^h(t)\right) = \\
& \int_{\Omega_{\tilde{t}}} \boldsymbol{\varepsilon}(\mathbf{w}_m^h) : \mathbf{D}^h \, \boldsymbol{\varepsilon}\left(\hat{\mathbf{y}}^h(t) - \hat{\mathbf{y}}^h(\tilde{t})\right) \, \mathrm{d}\Omega.
\end{aligned} \tag{11}
$$

Eq. (8) introduces the stabilization parameters τ_{SUPS} and ν_{LSIC}. These have been designed to provide good stability and optimal convergence of the discrete formulation through extensive studies [7–9, 11, 13, 14, 17, 19, 25, 41, 53, 72–83]. In this work we use the definitions given in [80]. In Eq. (10) τ_{TAN} and τ_{NOR} are boundary penalty parameters for the tangential and normal directions, respectively, as defined in [9], and $\left(\Gamma_t\right)_g^-$ is defined as the inflow part of $\left(\Gamma_t\right)_g$:

$$
\left(\Gamma_t\right)_g^- = \left\{\mathbf{x} | \left(\mathbf{u}^h - \hat{\mathbf{u}}^h\right) \cdot \mathbf{n} < 0, \forall \mathbf{x} \subset \left(\Gamma_t\right)_g\right\}. \tag{12}
$$

$\mathbf{r}_M$ and r_C are residuals of the linear-momentum and continuity differential equations, respectively, given by:

$$\mathbf{r}_M(\mathbf{u}^h, p^h) = \rho \left(\left. \frac{\partial \mathbf{u}^h}{\partial t} \right|_{\hat{x}} + \left(\mathbf{u}^h - \hat{\mathbf{u}}^h \right) \cdot \nabla \mathbf{u}^h - \mathbf{f}^h \right) \\ - \nabla \cdot \boldsymbol{\sigma} \left(\mathbf{u}^h, p^h \right), \tag{13}$$

$$\mathrm{r}_C(\mathbf{u}^h, p^h) = \nabla \cdot \mathbf{u}^h. \tag{14}$$

The fluid mesh part of the problem, Eq. (11), is the linear-elastic equation with the elastic tensor $\mathbf{D}^h$ defined on a "nearby configuration" $\Omega_{\tilde{t}}$ at time $\tilde{t} < t$. In practice, $\tilde{t}$ is taken at the previous time step. For mesh deformation we adopted Jacobian-based stiffening [55–57].

The fluid mesh displacements $\hat{\mathbf{y}}^h$ and velocities $\hat{\mathbf{u}}^h$ are prescribed on all boundaries. For a boundary, such as the bridge deck, that undergoes forced-vibration we have employed the boundary conditions as follows. Let $\hat{\mathbf{x}}^h_I$ and $\hat{\mathbf{x}}^h_{0,I}$ denote the reference coordinates of the fluid-object interface and its centroid, respectively. For an arbitrary rigid-body displacement $\hat{\mathbf{y}}^h_{0,I}(t)$ and rotation $\theta(t)$ of the centroid, the displacement of the interface $\hat{\mathbf{y}}^h_I(t)$ is taken as:

$$\hat{\mathbf{y}}^h_I(t) = \left(\mathbf{R}(\theta(t)) - \mathbf{I} \right) \left(\hat{\mathbf{x}}^h_I - \hat{\mathbf{x}}^h_{0,I} \right) + \hat{\mathbf{y}}^h_{0,I}(t) \tag{15}$$

where $\mathbf{R}\left(\theta(t)\right)$ is the rotation tensor. The fluid-object interface velocity $\hat{\mathbf{u}}^h_I$ is obtained by the time derivative of $\hat{\mathbf{y}}^h_I$.

We use the Generalized-α method (see [80, 84, 85]) for time integration of the ALE-VMS equations. Within each time step we perform a single mesh solve followed by predictor-multicorrector Newton–Raphson iterations for the fluid mechanics problem.

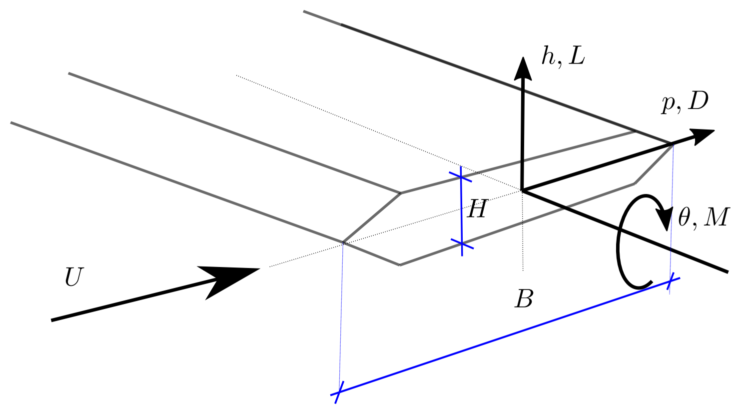

Figure 2: Aerodynamic forces on a bridge section.

4. Aeroelastic forces

With reference to quasi-steady theory [86] and the strip method [87], the aeroelastic forces on a line-like bluff body with width B and height H are given by the instantaneous drag, lift and pitching moment per unit length, denoted $D(t)$, $L(t)$ and $M(t)$, respectively. These are commonly given in terms of their dimensionless load coefficients, $C_D(t)$, $C_L(t)$ and $C_M(t)$, defined as:

$$C_D(t) = \frac{D(t)}{\frac{1}{2}\rho U^2 H}, \quad C_L(t) = \frac{L(t)}{\frac{1}{2}\rho U^2 B}, \quad C_M(t) = \frac{M(t)}{\frac{1}{2}\rho U^2 B^2}, \tag{16}$$

following the notation and conventions in Fig. 2. Fig. 2 also defines the three degrees-of-freedom p, h and θ with respect to the bridge deck centroid which defines the bridge deck motion. U is the mean wind velocity.

Following Theodorsen's theory [88], Scanlan and coworkers proposed an empirical expression for the motion-induced contribution to the aerodynamic forces [89], where the self-excited drag, lift and pitching moment, $D_{se}(t), L_{se}(t)$ and

$M_{se}(t)$, respectively, are given as:

$$D_{se} = \frac{1}{2}\rho U^2 BK\Big[P_1^*\frac{\dot{p}}{U} + P_5^*\frac{\dot{h}}{U} + P_2^*\frac{B\dot{\theta}}{U} + KP_4^*\frac{p}{B} + KP_6^*\frac{h}{B} + KP_3^*\theta\Big], \tag{17}$$

$$L_{se} = \frac{1}{2}\rho U^2 BK\Big[H_5^*\frac{\dot{p}}{U} + H_1^*\frac{\dot{h}}{U} + H_2^*\frac{B\dot{\theta}}{U} + KH_6^*\frac{p}{B} + KH_4^*\frac{h}{B} + KH_3^*\theta\Big], \tag{18}$$

$$M_{se} = \frac{1}{2}\rho U^2 B^2 K\Big[A_5^*\frac{\dot{p}}{U} + A_1^*\frac{\dot{h}}{U} + A_2^*\frac{B\dot{\theta}}{U} + KA_6^*\frac{p}{B} + KA_4^*\frac{h}{B} + KA_3^*\theta\Big], \tag{19}$$

where P_i^*, H_i^* and A_i^*, $i = \{1\,..\,6\}$ are the so-called aerodynamic derivatives [89–91]. These shape-dependent parameters may be regarded as transfer functions between body motion and self-excited forces, and are commonly expressed in conjunction with the reduced frequency, defined as $K = B\omega/U$, or the reduced velocity, $V_{red} = K^{-1}$, where ω is the angular frequency of the structural motion. These aerodynamic derivatives are essential to assess the dynamic performance and predict the critical wind speed of a dynamic system. Analogue to Eq. (16) it is convenient to express the self-excited forces in terms of normalized load coefficients, defined as:

$$C_{D,se} = \frac{D_{se}(t)}{\frac{1}{2}\rho U^2 H},\ C_{L,se} = \frac{L_{se}(t)}{\frac{1}{2}\rho U^2 B},\ C_{M,se} = \frac{M_{se}(t)}{\frac{1}{2}\rho U^2 B^2}. \tag{20}$$

As an alternative to the free-vibration wind tunnel experiment [92], the forced-vibration experiment [93] has proven to be an efficient and repeatable method to obtain the flutter characteristics of bridge sections [94, 95]. In this experiment the sectional model is driven in a user-defined motion by a vibration excitation system. The forces are simultaneously measured by force-transducers. A detailed description of the experimental setup is given in [71]. All experiments should however be considered with some uncertainty, as it has been pointed out in [96] that laboratory environment or operational conditions might have a non-negligible effect on the aeroelastic forces.

5. Analysis setup

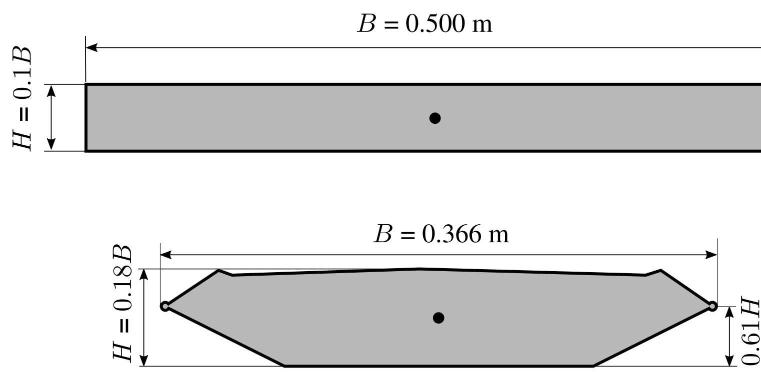

Figure 3: Cross sections considered. BH10: rectangular prism with aspect ratio B/H = 10 (above) and HAD3: 1:50 scaled model of the Hardanger bridge section (below).

The two sections shown in Fig. 3 are considered. The rectangular prism with aspect ratio B/H = 10, referred to as BH10, represents the classical example in the study of bluff body aerodynamics, and with its characteristic detached flows at the leading edge it is also often considered as a representative of many types of bridge sections. The other section is a 1:50 scale of the Hardanger bridge [61], referred to as HAD3. In this work we consider the ”clean deck”, without details as pavement and guide vanes. This model represents a new generation of suspension bridges with highly optimized aerodynamic design. Although this cross section is more streamlined, it still exhibit bluff body-like flow characteristics due to the high Reynold’s numbers.

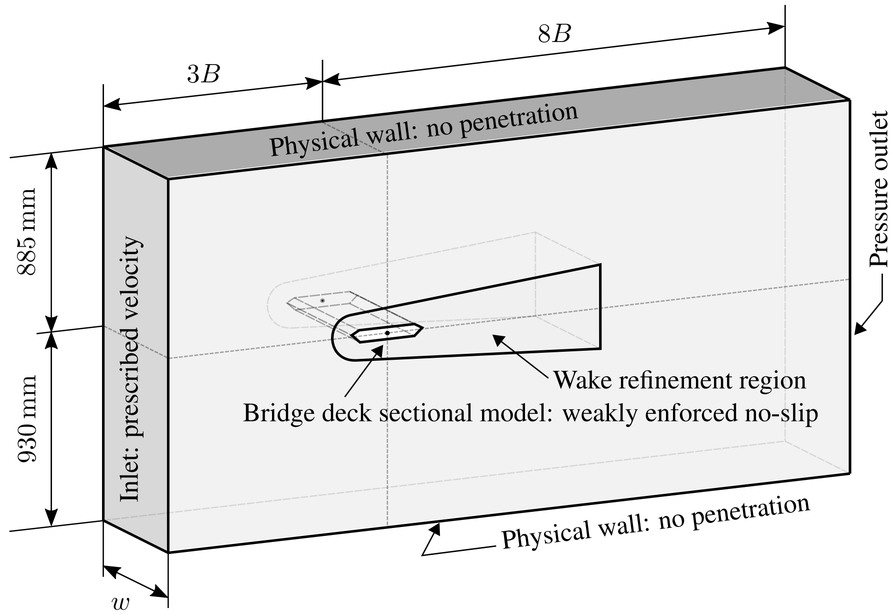

Figure 4: Outline of the computational domain showing dimensions and adopted boundary conditions.

The computational domain is taken as a box that represents a slice of the wind tunnel. The inflow and outflow surfaces are placed approximately $3B$ and $8B$ from the bridge deck centroid, respectively. For the upper and lower boundaries of the domain we have used the physical dimensions of the wind tunnel with a total height of 1815 mm and the deck centroid placed 930 mm above the floor, as shown in Fig. 4. The physical width of the wind tunnel, i.e. the length of the sectional model, is 2730 mm. The computational width is, however, reduced to 500 mm. In the parameter study in Sec. 6 this proves sufficiently wide to capture the three-dimensional flow structures, which were shown to have a non-negligible effect on the aerodynamic forces in [66] and [97].

For the fluid mechanics boundary conditions, smooth flow with wind velocity U is prescribed on the inflow surface. The walls, including the transverse bound-

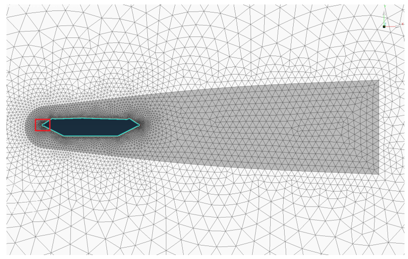

(a) Wake refinement region.

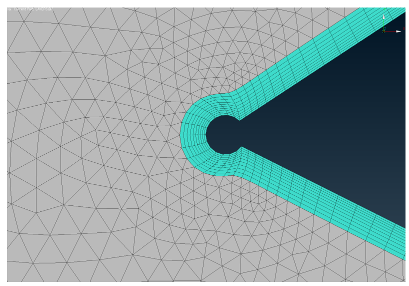

(b) Boundary layer elements.

Figure 5: Close-up view of the fluid mechanics mesh near the bridge deck.

aries, are constrained with no penetration, and on the bridge deck the weakly-enforced no-slip boundary condition is employed. The outflow surface is traction-free.

An interior surface enclosing the bridge deck, shown in Fig. 5a, defines a wake refinement region which is used to perform local mesh refinement and employ mesh moving boundary conditions. The wake refinement region is constrained by Eq. (15) to follow the vertical and horizontal motions of the bridge deck and rotate with half the magnitude. With this setup, mesh distortion is kept at a minimum while keeping the region of the refined mesh at the wake, even for relatively large rotations.

For discretization all surfaces are meshed with unstructured linear triangles. Prismatic elements extruded from the bridge deck surface define the boundary layers, as shown in Fig. 5b. In this work the number of boundary layers is set to 10. For the fluid mesh problem these elements are treated rigidly, which besides eliminating mesh distortion near the bridge deck also reduce the fluid mesh problem significantly, as the boundary layers typically constitute nearly half of the nodes in the computational model. The remaining volumes are meshed with linear tetrahedrons.

With a total grid size of 8.3×10^5 and 1.1×10^6 nodes for BH10 and HAD3, respectively, an effective computation relies on a parallel implementation. The computations in this work make use of the Message Passing Interface (MPI) libraries adopted from [98] and [99].

The air density, ρ, is set to $1.225\,\mathrm{kg/m^3}$ and the dynamic viscosity, μ, is set equal to $1.7894 \times 10^{-5}\,\mathrm{kg/ms}$. The computational time stepping has been set to approximately $1 \times 10^{-3}\,B/U$, giving a maximum Courant number below 2.5 at the smallest boundary layer elements.

The forced-vibration experiment is relatively easy to investigate numerically, as no momentum equations need to be solved for the structure and the fluid mechanics and the fluid mesh blocks can be solved separately. With the sectional model restricted to the three degree-of-freedom p, h and θ, with reference to Fig. 2, its motion can be described in the 2D ph-plane. With the strip method we also consider the bridge deck as a rigid body.

Following the wind tunnel experiments [71] we excite the sectional models in a single harmonic motion with amplitudes of 15 mm for p and h, and 2° for θ. For each motion we have studied wind velocities of U = 4 and 8 m/s and vibration frequencies of f_j = 1.1, 0.8 and 0.5 Hz, $j = \{p,\, h,\, \theta\}$, rendering reduced velocities, V_{red} between 1.2 and 7.0 and Reynolds numbers in the range of $1.0 - 2.0 \times 10^5$

for HAD3 and $1.4 - 2.7 \times 10^5$ for BH10. As a verification, some analyses are performed for other combinations of U and f giving the same V_{red}.

The self-excited forces are taken as the total aerodynamic forces detrended over the last whole number of displacement cycles. The aerodynamic derivatives are then identified by least squares fitting of Eqs. (17) – (19), as described in [71].

6. Results

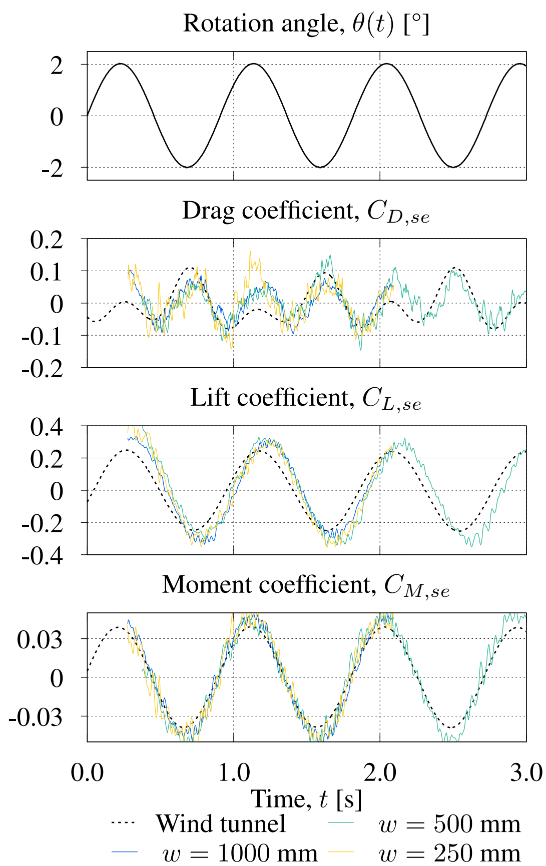

Figure 6: The effect of domain width on the self-excited force coefficients for BH10. $Re = 2.7 \times 10^5$, $V_{red} = 4.3$ ($U = 8$ m/s and $f_\theta = 1.1$ Hz).

In this section we present the numerical results. The aeroelastic forces are mainly given in terms of the normalized load coefficients (Eqs. (16) and (20)), or in terms of the aerodynamic derivatives. All comparisons between simulations and experiments are conducted with the self-excited forces due to inaccurate calibration of the absolute forces, which cancels out when the in-wind measurements are subtracted from the corresponding still-air measurements. To the experimental data, a numerical Buttersworth filter [100] with low-pass frequency of 3 Hz is applied to remove electrical noise and forces originating from vibration of the sectional models. This issue is closely discussed in [71]. For the simulations, however, where no such disturbances occur, we prefer to represent time series either without any numerical filters or with both the filtered and the unfiltered forces.

A parameter study of the domain width is presented in Fig. 6. From the insignificant difference between the self-excited forces for domain widths in the range of 250 to 1000 mm, it is evident that the three-dimensional effects are sufficiently captured for the present study. As a consequence of the decreasing correlation between the force fluctuations in the transverse direction, these become less evident with the increasing domain width. This effect is most clearly seen in drag comparing $w = 250$ mm and $w = 500$ mm. Throughout the rest of this work,the domain width is set to $w = 500$ mm.

To ensure that the self-excited forces from the numerical analyses can be regarded as a stationary process we start sampling them at a time period of approximately $t = 5.5B/U$ after the deck is set to motion. At this time the effects of the initial condition is no longer present in the case of non-moving decks and the forces pose stable behavior, as seen in Fig. 7. We have assumed that the same initialization time applies to the forced-vibration case. Note that for all analyses

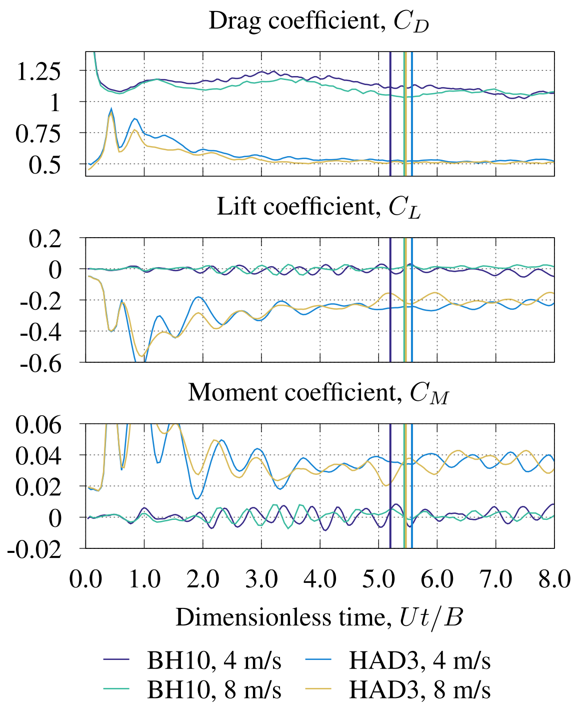

Figure 7: Development of total forces on BH10 and HAD3 with various wind speeds for a stationary simulation. The initial conditions, i.e. at $t = 0$, the flow is uniform in the entire domain.

the simulation is run for 1 s before the deck is set in motion. The aerodynamic derivatives are computed from two cycles, which in [101] has proven to be a good compromise between accuracy and computational efficiency.

We do not present any full convergence study herein. However, in Fig. 8 the self-excited forces for a selected forced-vibration analysis (BH10 with $U = 8$ m/s and $f_\theta = 1.1$ Hz) are compared using half the time step ($\Delta t/2$), and doubled mesh density also using half the time step (Δt, Refined). The latter yield a Courant number approximately equal to the original analysis. The results are indistinguishable and suggest that the numerical solution has converged.

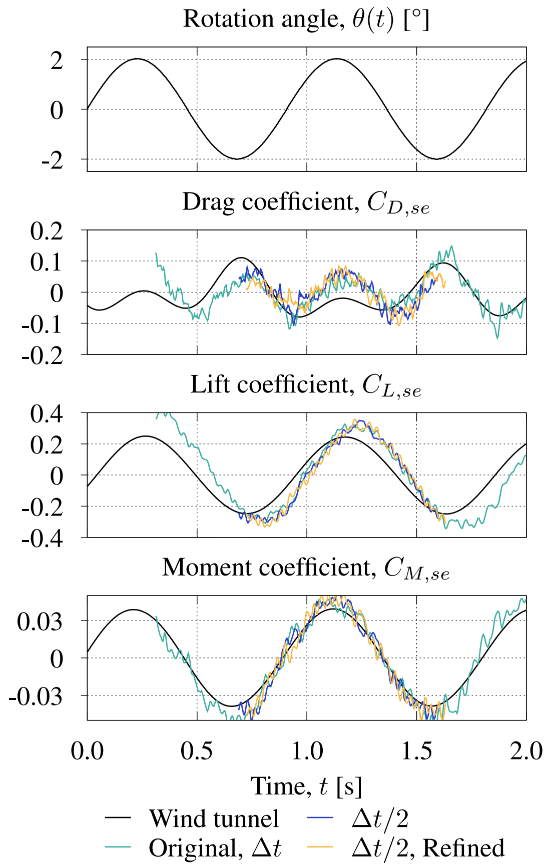

Figure 8: Convergence with respect to computational time stepping and mesh refinement of self-excited forces for the BH10 section with $V_{red} = 2.3$ ($U = 8$ m/s and $f_\theta = 1.1$ Hz).

6.1. The role of weakly-enforced essential boundary conditions

To demonstrate the ability of the ALE-VMS method with weakly-enforced BCs to deal with relatively coarse boundary meshes on bluff body aerodynamics we have employed both the classical strongly-enforced, and the weakly-enforced no-slip boundary conditions on a forced-vibration simulation of the HAD3 section. For this study we take the original mesh setup described in Sec. 5 as the reference analysis and compare with a relatively coarse mesh without the prismatic boundary layer elements. On this mesh the number of nodes is reduced by

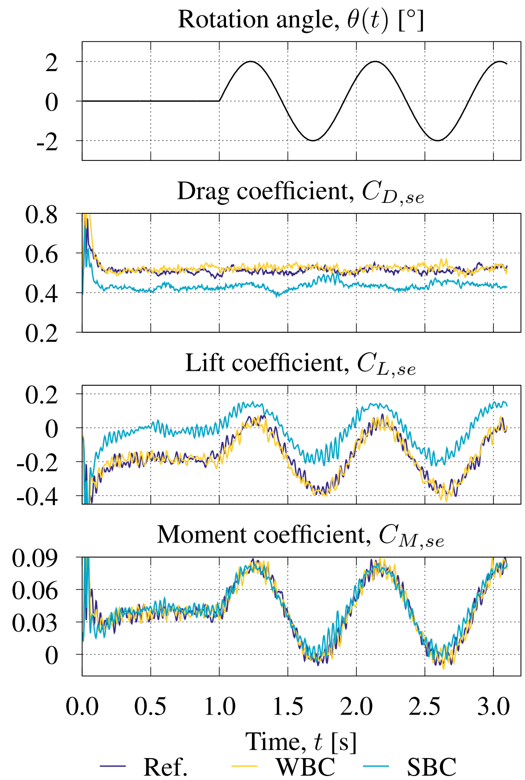

Figure 9: Load coefficients HAD3 at $Re = 2 \times 10^5$ with $U = 8$ m/s, f_θ = 1.1 Hz and $w = 500$ mm obtained with weakly- and strongly-enforced BCs (WBC and SBC, respectively) for a coarse mesh. Reference solution represents a fine mesh with strongly-enforced BCs.

85 % to 150×10^3 nodes.

Fig. 9 shows the total load coefficients for drag, lift and pitching moment for the pitching mode with $V_{red} = 3.2$ ($f_\theta = 1.1$ Hz and $U = 8$ m/s) and unsurprisingly, the weak BCs outperform the strong in terms of accuracy. While the strong BCs underestimate the magnitudes of both drag and lift for such coarse discretizations, the weakly-enforced BCs captures the reference solution with very good accuracy.

The strong BCs forms artificially thick boundary layers retarding the flow and

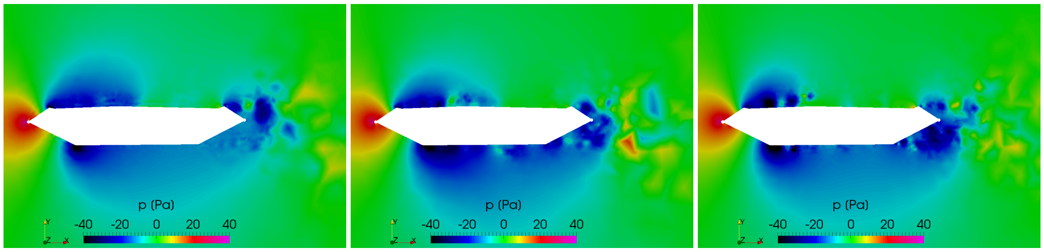

(a) SBC. **(b)** WBC. **(c)** Reference.

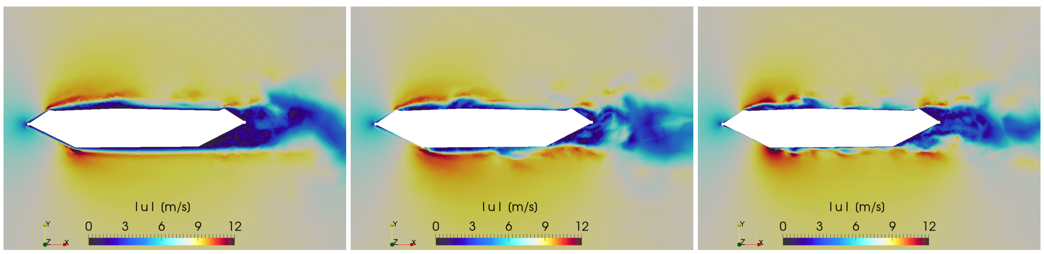

(d) SBC. **(e)** WBC. **(f)** Reference.

Figure 10: Pressure (top) and air speed contours (bottom) for HAD3 at $t = 2.40$s for the $u = 8$ m/s and $f = 1.1$ Hz forced vibration simulation. (a) and (d): Strongly-enforced BCs (SBC), (b) and (e): Weakly-enforced BCs (WBC), (c) and (f): Reference analysis.

makes it behave more viscous. The weak BCs, however, let instead the flow slip on the surface without forming undesirably thick boundary layers. In this way the pressure distribution, which dominates the aerodynamic forces, as well as the turbulent structures, becomes more realistic. This is clearly seen in Fig. 10 where pressure and air speed contours for a snapshot at $t = 2.40$ s are shown for the two methods.

Remark 1. It should be remarked that although we see a significant difference using weak and strong BCs for bluff bodies, earlier work [23] has found that for streamlined bodies like airfoils where the flows are fully attached, the gain using weakly-enforced BCs might be even larger.

Remark 2. The mesh used in this study is artificially coarse and for the model-scale geometrically clean sections studied in this work, the difference between weakly- and strongly-enforced BCs becomes less significant. The example does however show the supremacy of the weakly-enforced BCs for cases where sufficient boundary layer resolution is unaffordable, e.g. for complex geometries with pavements, spoilers, etc. and full-scale simulations with extremely high Reynold's numbers.

6.2. Flutter derivatives for BH10

For the BH10 section, the numerically computed aerodynamic derivatives governing the self-excited drag, lift and pitching moment are shown in Figs. 11, 12 and 13, respectively. The same plots also show the experimental results, for which the dashed lines represent their least-square fitted 3rd order polynomial curve. For the drag-related aerodynamic derivatives P_i^* the numerical results we get a nice representation of the harmonic component related to lateral motion p, i.e. P_4^* and P_1^*, which is the most important flutter derivative concerning drag. For the pitching motion the experiments reveal a very non-physical behavior for P_3^*. For this symmetrical cross section subjected to a pitching motion we would expect a symmetrical response with double frequency in drag. The experimental P_3^* do however contain a distinct harmonic component. This error typically arise from calibration of zero angle-of-attack. In the simulations the drag response is symmetric with respect to positive and negative angle-of-attack, giving P_2^* and P_3^* equal to zero. This is clearly seen in the time series in Fig. 14, showing the self-excited forces for $U = 8$ m/s and f_θ = 0.5 Hz.

For the H^*- type aerodynamic derivatives we observe fair agreement between experiments and simulations for low values of V_{red}. However, for lower frequencies the deviations increase, especially for H_4^* and H_2^* indicating a difference in phase of the self-excited forces between simulations and experiments. Moreover, the simulations consequently render higher force magnitudes for both the vertical and the pitching motion towards the stationary limit. Earlier work on the same section have made the same observations, see e.g. [62, 63].

Regarding the pitching moment and their A^*-type aerodynamic derivatives the experiments are reproduced with better accuracy although the observations made for lift are also seen here, however less prominent. The time series used to compute the aerodynamic derivatives related to pitching- and vertical motion for $V_{red} = 5.1$ are respectively shown in Figs. 14 and 15.

Remark 3. One should keep in mind that because the self-excited drag is vanishingly small, both compared to the lifting force and forces arising from structural vibration of the sectional model, it is very difficult to separate from the total measured forces. As lift and pitching moment dominate the self-excited forces, the lateral forces and motions are in fact often disregarded in flutter analyses. This may however lead to underestimation of the critical flutter wind speed, as pointed out in [102].

6.3. Flutter derivatives for HAD3

As for BH10, the aerodynamic derivatives for the HAD3 section are presented in Figs. 16, 17 and 18 for self-excited drag, lift and pitching moment, respectively. For this section there is generally very good agreement between simulations and experiments, and particularly for those that have been pointed out as the most important in flutter analysis [102]; A_1^*, A_2^*, A_3^* and H_1^*. Higher magnitudes of the lift and the pitching moment are also seen for this section, however less distinct than for BH10. We also observe that excellent agreement is obtained for the phase angles, i.e. the ratio between aerodynamic derivatives related to the structural motion and its time derivative. This is clearly illustrated in the time series in Fig. 19, showing the self-excited forces for $U = 8$ m/s and $f_\theta = 0.5$ Hz.

The self-excited drag is mainly governed by the lateral velocity through P_1^* and is in good agreement with the experiments. The experimental drag forces are however, as pointed out in Sec. 6.2, due to their small magnitude associated with a lot of uncertainty.

An interesting observation in the simulations is the action of the lateral motion on the pitching moment, i.e. A_6^*. To some extent the same effect is seen for the lifting force in terms of H_5^* and H_6^* for experiments and simulations, however, the experiments do not capture this effect for the pitching moment. Fig. 20, showing the self-excited forces for $U = 8$ m/s and $f_p = 0.8$ Hz, supports this observation.

7. Conclusions

In this paper a methodology to perform the forced-vibration experiment using ALE-VMS techniques augmented with weak enforcement of the essential boundary conditions has been presented. The problem is solved very effectively in a blockwise fashion with a mesh-moving algorithm that reduces the fluid mesh problem significantly.

It has been shown that in the case of coarsely discretized boundary layers, the weakly-enforced BCs outperform the classical no-slip. Instead of forming artificially thick boundary layers and flow retardation, the flow is allowed to slip on the surface and represent the pressure field and turbulent patterns more accurate. Although an artificially coarse mesh was used to illustrate this, the example clearly show the ability of the formulation to accurately represent the aerodynamic forces in cases where optimal mesh resolution is impossible.

Using the forced-vibration method, complete aerodynamic derivatives for lateral, vertical and pitching degrees-of-freedom have been computed for two bridge deck sectional models numerically. Wind tunnel experiments of the same sections have been performed and used for comparison. The setup of the numerical simulations was chosen to match the experiments as closely as possible in order to compare not only the aerodynamic derivatives, but also the time series from which they are computed. The BH10 show fair agreement between simulations and experiments. However, clear discrepancies appear in the region of high reduced velocities and especially H_4^* and H_2^* manifest that the structural velocity is of different importance in the experiments and the simulations. For the HAD3 section the numerically obtained aerodynamic derivatives closely match the experimental, even for high V_{red}. However, although less distinct than for BH10, also this section render higher self-excited forces in the simulations, especially for the pitching moment.

Because of its computational effectiveness and user-friendly problem definition, we believe the proposed method represents a beneficial tool in aeroelastic analysis of bridges. However, open questions remain regarding the discrepancies in aerodynamic derivatives for high reduced velocities, especially prominent for the rectangular prism, which encourage further investigations.

8. Acknowledgment

This work was carried out with financial support from the Norwegian Public Roads Administration (NPRA). All simulations were performed on resources provided by UNINETT Sigma2 - the National Infrastructure for High Performance Computing and Data Storage in Norway. YB was partially supported by ARO Grant No. W911NF-14-1-0296 and AK was partially supported by the Natural Sciences and Engineering Research Council of Canada (NSERC), funding reference number RGPIN-2017-03781. The authors greatly acknowledge this support.

We would also like to thank Bartosz Siedziako and Bjørn Schjølberg from Department of Structural Engineering, NTNU, for performing the wind tunnel experiments.

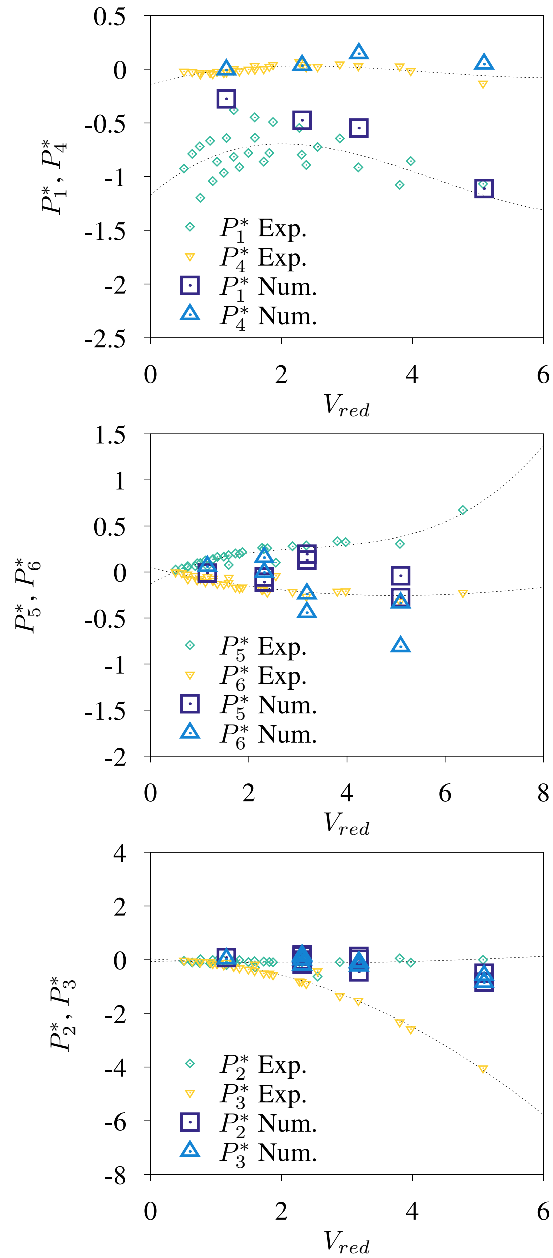

Figure 11: BH10 aerodynamic derivatives governing self-excited drag.

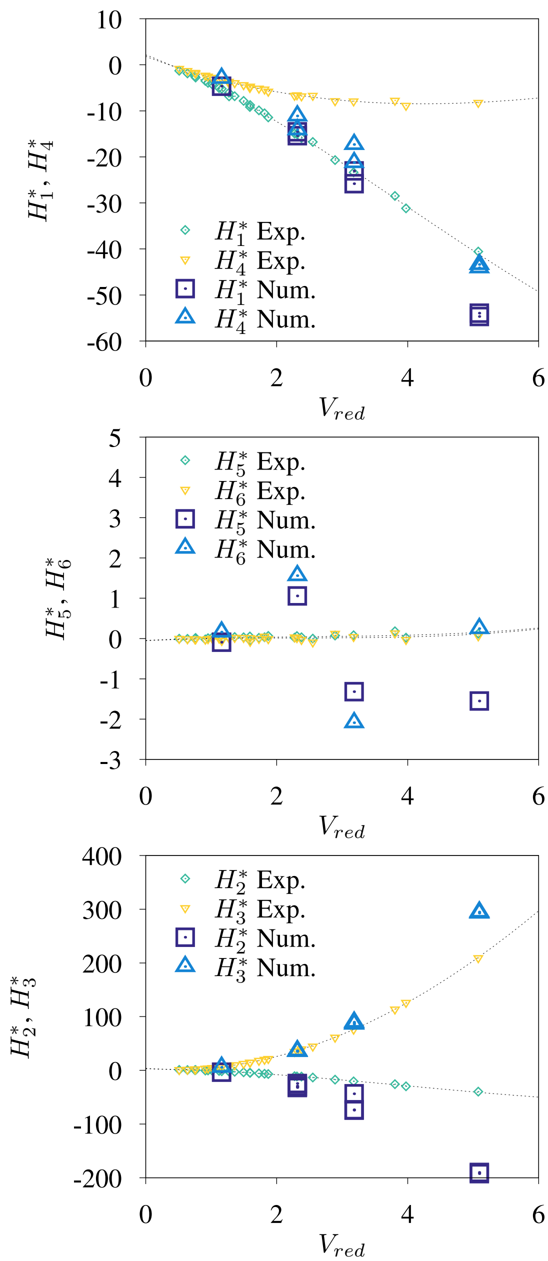

Figure 12: BH10 aerodynamic derivatives governing self-excited lift.

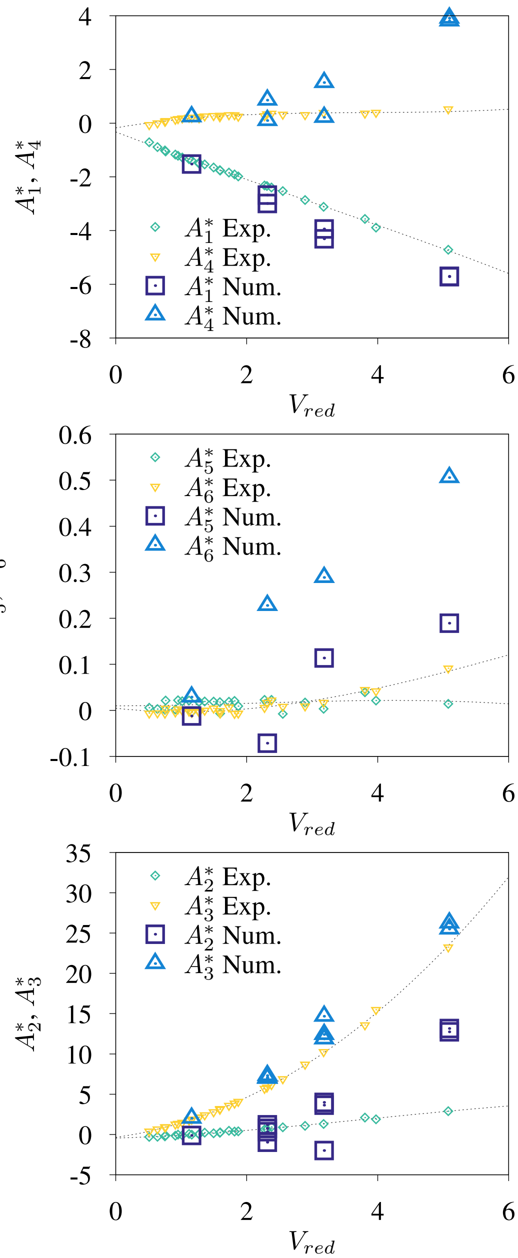

Figure 13: BH10 aerodynamic derivatives governing self-excited pitching moment.

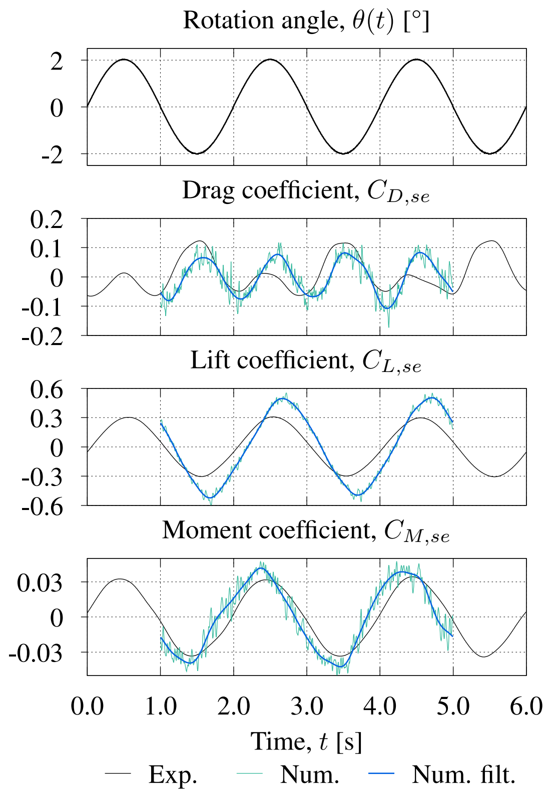

Figure 14: Filtered and unfiltered self-excited force coefficients for the BH10 section (Num. and Num. filt., respectively) for $V_{red} = U/B\omega = 5.1$ ($U = 8$ m/s and $f_\theta = 0.5$ Hz, $Re = 2.7 \times 10^5$) compared with the corresponding wind tunnel time series (Exp.).

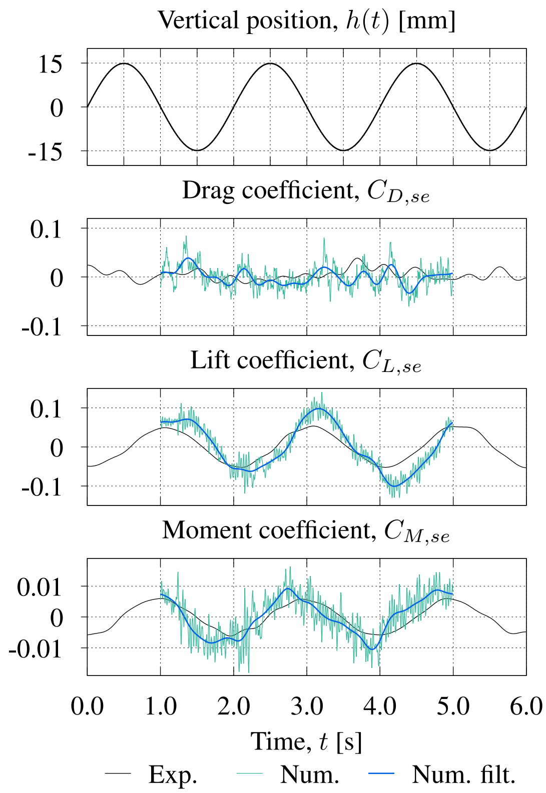

Figure 15: Filtered and unfiltered self-excited force coefficients for the BH10 section (Num. and Num. filt., respectively) for $V_{red} = 5.1$ ($U = 8$ m/s and $f_h = 0.5$ Hz, $Re = 2.7 \times 10^5$) compared with the corresponding wind tunnel time series (Exp.).

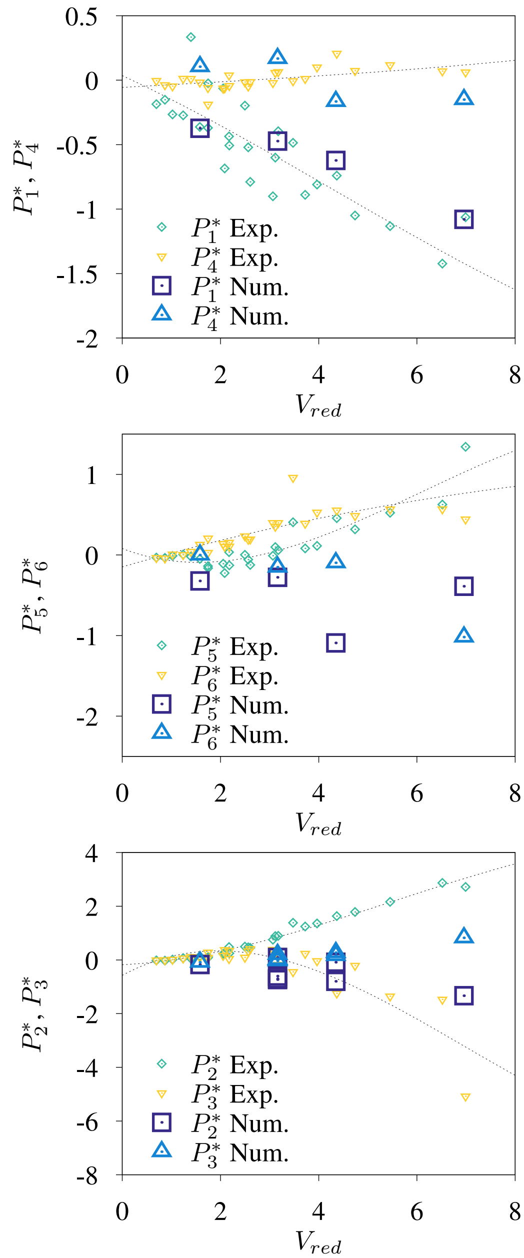

Figure 16: HAD3 aerodynamic derivatives governing self-excited drag.

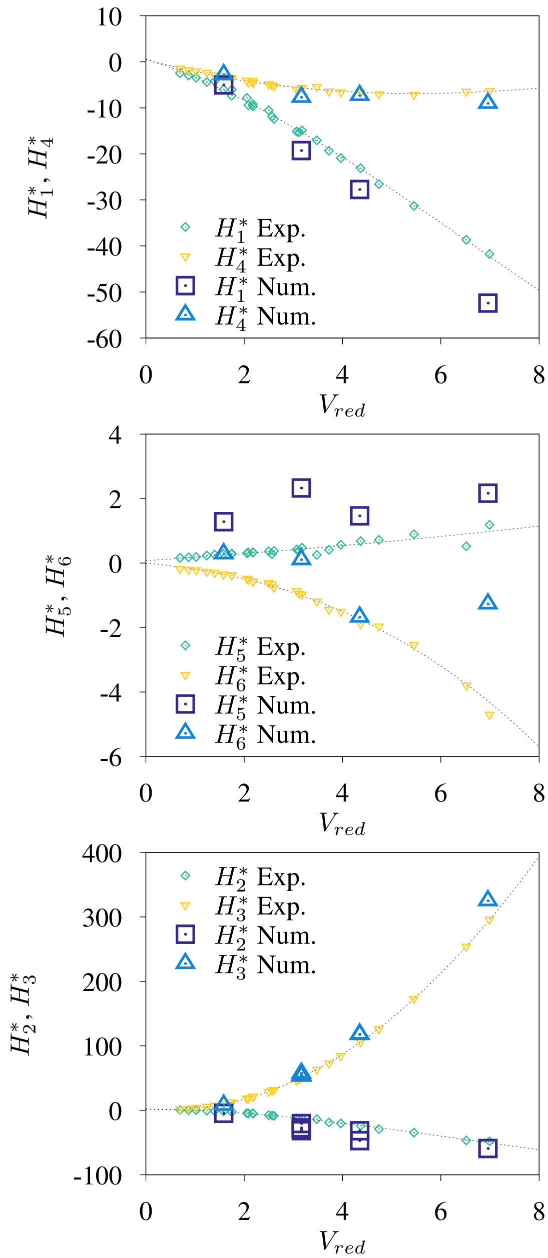

Figure 17: HAD3 aerodynamic derivatives governing self-excited lift.

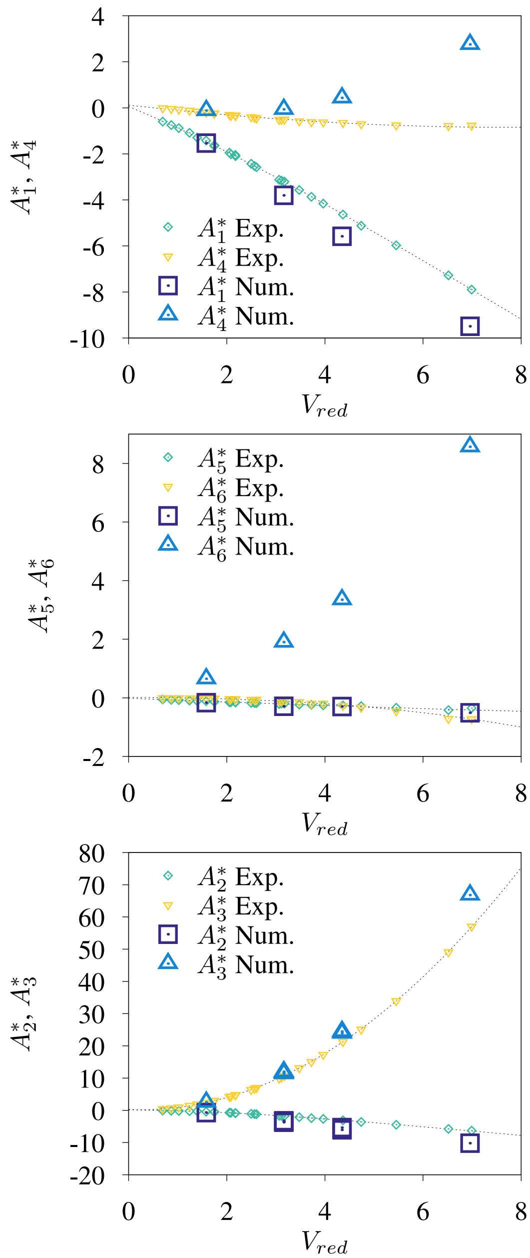

Figure 18: HAD3 aerodynamic derivatives governing self-excited pitching moment.

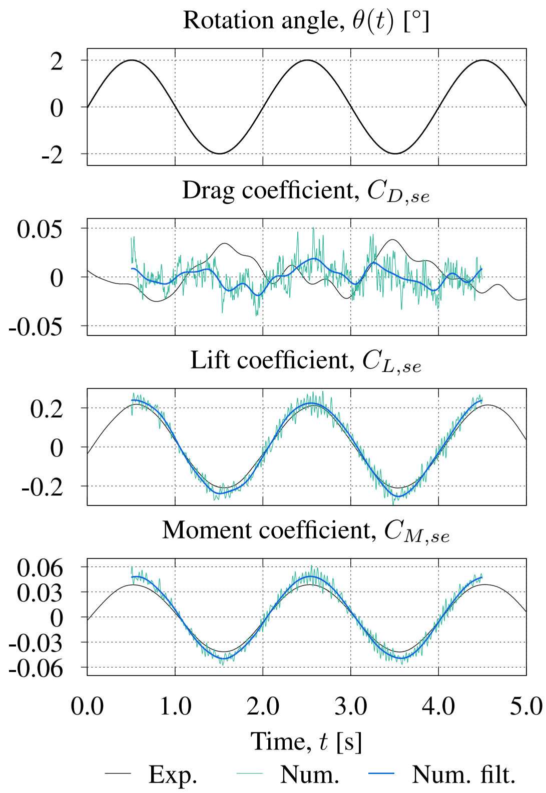

Figure 19: Filtered and unfiltered self-excited force coefficients for the HAD3 section (Num. and Num. filt., respectively) for $V_{red} = 7.0$ ($U = 8$ m/s and $f_\theta = 0.5$ Hz, $Re = 2.0 \times 10^5$) compared with the corresponding wind tunnel time series (Exp.).

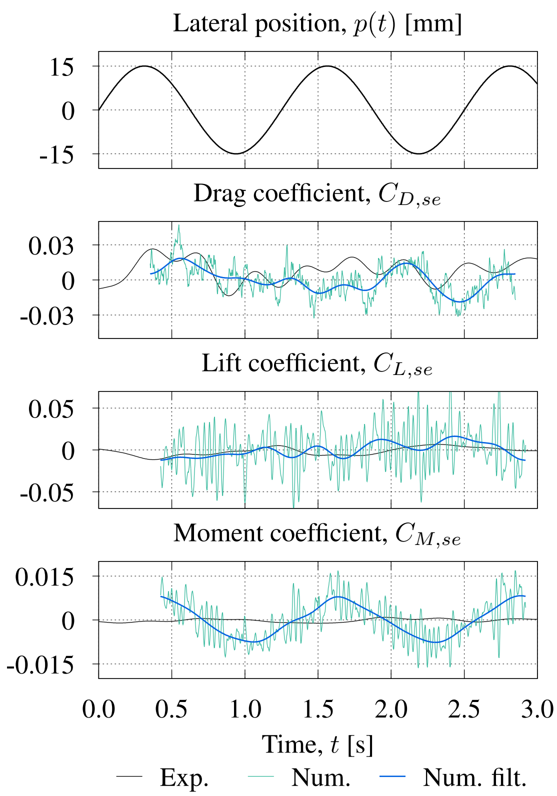

Figure 20: Filtered and unfiltered self-excited force coefficients for the HAD3 section (Num. and Num. filt., respectively) for $V_{red} = 4.3$ ($U = 8$ m/s and $f_p = 0.8$ Hz, $Re = 2.0 \times 10^5$) compared with the corresponding wind tunnel time series (Exp.).

[1] Y. Bazilevs, M.-C. Hsu, K. Takizawa, T. E. Tezduyar, ALE-VMS and ST-VMS methods for computer modeling of wind-turbine rotor aerodynamics and fluid–structure interaction, Mathematical Models and Methods in Applied Sciences 22 (supp02) (2012) 1230002. doi:10.1142/S0218202512300025.

[2] Y. Bazilevs, K. Takizawa, T. E. Tezduyar, Challenges and directions in computational fluid–structure interaction, Mathematical Models and Methods in Applied Sciences 23 (2013) 215–221. doi:10.1142/S0218202513400010.

[3] Y. Bazilevs, K. Takizawa, T. Tezduyar, M.-C. Hsu, N. Kostov, S. McIntyre, Aerodynamic and FSI analysis of wind turbines with the ALE-VMS and ST-VMS methods, Archives of Computational Methods in Engineering 21 (2014) 359–398.

[4] K. Takizawa, Y. Bazilevs, T. E. Tezduyar, C. C. Long, A. L. Marsden, K. Schjodt, ST and ALE-VMS methods for patient-specific cardiovascular fluid mechanics modeling, Mathematical Models and Methods in Applied Sciences 24 (2014) 2437–2486.

[5] Y. Bazilevs, K. Takizawa, T. Tezduyar, New directions and challenging computations in fluid dynamics modeling with stabilized and multiscale methods., Mathematical Models and Methods in Applied Sciences 25 (2015) 2217–2226.

[6] Y. Bazilevs, A. Korobenko, J. Yan, A. Pal, S. Gohari, S. Sarkar, ALE–VMS formulation for stratified turbulent incompressible flows with applications,

Mathematical Models and Methods in Applied Sciences 25 (12) (2015) 2349–2375.

[7] Y. Bazilevs, T. J. R. Hughes, Weak imposition of Dirichlet boundary conditions in fluid mechanics, Computers and Fluids 36 (2007) 12–26.

[8] Y. Bazilevs, C. Michler, V. M. Calo, T. J. R. Hughes, Isogeometric variational multiscale modeling of wall-bounded turbulent flows with weakly enforced boundary conditions on unstretched meshes, Computer Methods in Applied Mechanics and Engineering 199 (2010) 780–790.

[9] Y. Bazilevs, C. Michler, V. M. Calo, T. J. R. Hughes, Weak Dirichlet boundary conditions for wall-bounded turbulent flows, Computer Methods in Applied Mechanics and Engineering 196 (2007) 4853–4862.

[10] R. Golshan, A. Tejada-Martínez, M. Juha, Y. Bazilevs, Large-eddy simulation with near-wall modeling using weakly enforced no-slip boundary conditions, Computers & Fluids 118 (2015) 172–181.

[11] K. Takizawa, T. E. Tezduyar, H. Mochizuki, H. Hattori, S. Mei, L. Pan, K. Montel, Space–time VMS method for flow computations with slip interfaces (ST-SI), Mathematical Models and Methods in Applied Sciences 25 (2015) 2377–2406. doi:10.1142/S0218202515400126.

[12] K. Takizawa, T. E. Tezduyar, T. Kuraishi, S. Tabata, H. Takagi, Computational thermo-fluid analysis of a disk brake, Computational Mechanics 57 (2016) 965–977. doi:10.1007/s00466-016-1272-4.

[13] Y. Bazilevs, V. M. Calo, J. A. Cottrel, T. J. R. Hughes, A. Reali, G. Scovazzi, Variational multiscale residual-based turbulence modeling for large

eddy simulation of incompressible flows, Computer Methods in Applied Mechanics and Engineering 197 (2007) 173–201.

[14] Y. Bazilevs, I. Akkerman, Large eddy simulation of turbulent Taylor–Couette flow using isogeometric analysis and the residual–based variational multiscale method, Journal of Computational Physics 229 (2010) 3402–3414.

[15] J. Yan, A. Korobenko, A. Tejada-Martinez, R. Golshan, Y. Bazilevs, A new variational multiscale formulation for stratified incompressible turbulent flows, Computers & Fluids 158 (2017) 150–156.

[16] T. J. R. Hughes, W. K. Liu, T. K. Zimmermann, Lagrangian-Eulerian finite element formulation for incompressible viscous flows, Computer Methods in Applied Mechanics and Engineering 29 (3) (1981) 329–349. doi:10.1016/0045-7825(81)90049-9.

[17] Y. Bazilevs, K. Takizawa, T. E. Tezduyar, Computational Fluid–Structure Interaction: Methods and Applications, Wiley, 2013.

[18] A. Korobenko, M.-C. Hsu, I. Akkerman, Y. Bazilevs, Aerodynamic simulation of vertical-axis wind turbines, Journal of Applied Mechanics 81(2) (2013) 021011. doi:10.1115/1.4024415.

[19] M.-C. Hsu, I. Akkerman, Y. Bazilevs, Wind turbine aerodynamics using ALE–VMS: validation and the role of weakly enforced boundary conditions, Computational Mechanics 50 (4) (2012) 499–511. doi:10.1007/s00466-012-0686-x.

[20] J. Yan, B. Augier, A. Korobenko, J. Czarnowski, G. Ketterman, Y. Bazilevs, FSI modeling of a propulsion system based on compliant hydrofoils in a tandem configuration, Computers & Fluids 141 (2016) 201–211. doi:10.1016/j.compfluid.2015.07.013.

[21] I. Akkerman, J. Dunaway, J. Kvandal, J. Spinks, Y. Bazilevs, Toward free-surface modeling of planing vessels: simulation of the Fridsma hull using ALE-VMS, Computational Mechanics 50 (2012) 719–727.

[22] I. Akkerman, Y. Bazilevs, D. J. Benson, M. W. Farthing, C. E. Kees, Free-surface flow and fluid–object interaction modeling with emphasis on ship hydrodynamics, Journal of Applied Mechanics 79 (2012) 010905.

[23] M.-C. Hsu, D. Kamensky, Y. Bazilevs, M. S. Sacks, T. J. R. Hughes, Fluid–structure interaction analysis of bioprosthetic heart valves: significance of arterial wall deformation, Computational Mechanics 54 (2014) 1055–1071. doi:10.1007/s00466-014-1059-4.

[24] D. Kamensky, M.-C. Hsu, D. Schillinger, J. Evans, A. Aggarwal, Y. Bazilevs, M. Sacks, T. Hughes, An immersogeometric variational framework for fluid–structure interaction: Application to bioprosthetic heart valves, Computer Methods in Applied Mechanics and Engineering 284 (2015) 1005–1053.

[25] K. Takizawa, T. E. Tezduyar, S. McIntyre, N. Kostov, R. Kolesar, C. Habluetzel, Space–time VMS computation of wind-turbine rotor and tower aerodynamics, Computational Mechanics 53 (2014) 1–15. doi:10.1007/s00466-013-0888-x.

[26] K. Takizawa, Computational engineering analysis with the new-generation space–time methods, Computational Mechanics 54 (2014) 193–211. doi:10.1007/s00466-014-0999-z.

[27] K. Takizawa, B. Henicke, A. Puntel, N. Kostov, T. E. Tezduyar, Computer modeling techniques for flapping-wing aerodynamics of a locust, Computers & Fluids 85 (2013) 125–134. doi:10.1016/j.compfluid.2012.11.008.

[28] K. Takizawa, T. E. Tezduyar, N. Kostov, Sequentially-coupled space–time FSI analysis of bio-inspired flapping-wing aerodynamics of an MAV, Computational Mechanics 54 (2014) 213–233. doi:10.1007/s00466-014-0980-x.

[29] K. Takizawa, T. E. Tezduyar, A. Buscher, Space–time computational analysis of MAV flapping-wing aerodynamics with wing clapping, Computational Mechanics 55 (2015) 1131–1141. doi:10.1007/s00466-014-1095-0.

[30] K. Takizawa, K. Schjodt, A. Puntel, N. Kostov, T. E. Tezduyar, Patient-specific computer modeling of blood flow in cerebral arteries with aneurysm and stent, Computational Mechanics 50 (2012) 675–686. doi:10.1007/s00466-012-0760-4.

[31] K. Takizawa, K. Schjodt, A. Puntel, N. Kostov, T. E. Tezduyar, Patient-specific computational analysis of the influence of a stent on the unsteady flow in cerebral aneurysms, Computational Mechanics 51 (2013) 1061–1073. doi:10.1007/s00466-012-0790-y.

[32] K. Takizawa, T. E. Tezduyar, A. Buscher, S. Asada, Space–time fluid mechanics computation of heart valve models, Computational Mechanics 54 (2014) 973–986. doi:10.1007/s00466-014-1046-9.

[33] H. Suito, K. Takizawa, V. Q. H. Huynh, D. Sze, T. Ueda, FSI analysis of the blood flow and geometrical characteristics in the thoracic aorta, Computational Mechanics 54 (2014) 1035–1045. doi:10.1007/s00466-014-1017-1.

[34] K. Takizawa, D. Montes, S. McIntyre, T. E. Tezduyar, Space–time VMS methods for modeling of incompressible flows at high Reynolds numbers, Mathematical Models and Methods in Applied Sciences 23 (2013) 223–248. doi:10.1142/s0218202513400022.

[35] K. Takizawa, D. Montes, M. Fritze, S. McIntyre, J. Boben, T. E. Tezduyar, Methods for FSI modeling of spacecraft parachute dynamics and cover separation, Mathematical Models and Methods in Applied Sciences 23 (2013) 307–338. doi:10.1142/S0218202513400058.

[36] K. Takizawa, T. E. Tezduyar, J. Boben, N. Kostov, C. Boswell, A. Buscher, Fluid–structure interaction modeling of clusters of spacecraft parachutes with modified geometric porosity, Computational Mechanics 52 (2013) 1351–1364. doi:10.1007/s00466-013-0880-5.

[37] K. Takizawa, T. E. Tezduyar, A. Buscher, S. Asada, Space–time interface-tracking with topology change (ST-TC), Computational Mechanics 54 (4) (2014) 955–971. doi:10.1007/s00466-013-0935-7.

[38] K. Takizawa, T. E. Tezduyar, C. Boswell, R. Kolesar, K. Montel, FSI modeling of the reefed stages and disreefing of the Orion spacecraft parachutes, Computational Mechanics 54 (2014) 1203–1220. doi:10.1007/s00466-014-1052-y.

[39] K. Takizawa, T. E. Tezduyar, C. Boswell, Y. Tsutsui, K. Montel, Special methods for aerodynamic-moment calculations from parachute FSI modeling, Computational Mechanics 55 (2015) 1059–1069. doi:10.1007/s00466-014-1074-5.

[40] K. Takizawa, T. E. Tezduyar, R. Kolesar, FSI modeling of the Orion spacecraft drogue parachutes, Computational Mechanics 55 (2015) 1167–1179. doi:10.1007/s00466-014-1108-z.

[41] K. Takizawa, T. E. Tezduyar, T. Kuraishi, Multiscale ST methods for thermo-fluid analysis of a ground vehicle and its tires, Mathematical Models and Methods in Applied Sciences 25 (2015) 2227–2255. doi:10.1142/S0218202515400072.

[42] K. Takizawa, T. E. Tezduyar, New directions in space–time computational methods, in: Y. Bazilevs, K. Takizawa (Eds.), Advances in Computational Fluid–Structure Interaction and Flow Simulation: New Methods and Challenging Computations, Modeling and Simulation in Science, Engineering and Technology, Springer, 2016, pp. 159–178. doi:10.1007/978-3-319-40827-9_13.

[43] K. Takizawa, T. E. Tezduyar, Y. Otoguro, T. Terahara, T. Kuraishi, H. Hattori, Turbocharger flow computations with the Space–Time Isogeomet-

ric Analysis (ST-IGA), Computers and Fluids 142 (2017) 15–20. doi:10.1016/j.compfluid.2016.02.021.

[44] K. Takizawa, T. E. Tezduyar, S. Asada, T. Kuraishi, Space–time method for flow computations with slip interfaces and topology changes (ST-SI-TC), Computers & Fluids 141 (2016) 124–134. doi:10.1016/j.compfluid.2016.05.006.

[45] K. Takizawa, T. E. Tezduyar, T. Terahara, Ram-air parachute structural and fluid mechanics computations with the Space–Time Isogeometric Analysis (ST-IGA), Computers & Fluids 141 (2016) 191–200. doi:10.1016/j.compfluid.2016.05.027.

[46] Y. Bazilevs, A. Korobenko, X. Deng, J. Yan, Fluid–structure interaction modeling for fatigue-damage prediction in full-scale wind-turbine blades, Journal of Applied Mechanics 83 (6) (2016) 061010.

[47] J. Yan, A. Korobenko, X. Deng, Y. Bazilevs, Computational free-surface fluid–structure interaction with application to floating offshore wind turbines, Computers & Fluids 141 (2016) 155–174.

[48] J. Yan, X. Deng, A. Korobenko, Y. Bazilevs, Free-surface flow modeling and simulation of horizontal-axis tidal-stream turbines, Computers & Fluids 158 (2017) 157–166.

[49] A. Korobenko, J. Yan, S. Gohari, S. Sarkar, Y. Bazilevs, FSI Simulation of two back-to-back wind turbines in atmospheric boundary layer flow, Computers & Fluids 158 (2017) 167–175. doi:10.1016/j.compfluid.2017.05.010.

[50] K. Takizawa, T. E. Tezduyar, T. Terahara, T. Sasaki, Heart valve flow computation with the integrated Space–Time VMS, Slip Interface, Topology Change and Isogeometric Discretization methods, Computers & Fluids 158 (2017) 176–188. doi:10.1016/j.compfluid.2016.11.012.

[51] K. Takizawa, T. E. Tezduyar, H. Hattori, Computational analysis of flow-driven string dynamics in turbomachinery, Computers & Fluids 142 (2017) 109–117. doi:doi:10.1016/j.compfluid.2016.02.019.

[52] Y. Otoguro, K. Takizawa, T. E. Tezduyar, Space–time VMS computational flow analysis with isogeometric discretization and a general-purpose NURBS mesh generation method, Computers & Fluids 158 (2017) 189–200. doi:10.1016/j.compfluid.2017.04.017.

[53] K. Takizawa, T. E. Tezduyar, Y. Otoguro, Stabilization and discontinuity-capturing parameters for space–time flow computations with finite element and isogeometric discretizations, Computational Mechanics, published online (apr 2018). doi:10.1007/s00466-018-1557-x.

[54] R. Scotta, M. Lazzari, E. Stecca, J. Cotela, R. Rossi, Numerical wind tunnel for aerodynamic and aeroelastic characterization of bridge deck sections, Computers and Structures 167 (2016) 96–114. doi:10.1016/j.compstruc.2016.01.012.

[55] T. E. Tezduyar, M. Behr, S. Mittal, A. A. Johnson, Computation of unsteady incompressible flows with the finite element methods – space–time formulations, iterative strategies and massively parallel implementations, in: New

Methods in Transient Analysis, PVP-Vol.246/AMD-Vol.143, ASME, New York, 1992, pp. 7–24.

[56] T. Tezduyar, S. Aliabadi, M. Behr, A. Johnson, S. Mittal, Parallel finite-element computation of 3D flows, Computer 26 (10) (1993) 27–36. doi:10.1109/2.237441.

[57] A. A. Johnson, T. E. Tezduyar, Mesh update strategies in parallel finite element computations of flow problems with moving boundaries and interfaces, Computer Methods in Applied Mechanics and Engineering 119 (1994) 73–94. doi:10.1016/0045-7825(94)00077-8.

[58] T. Tezduyar, Finite element interface-tracking and interface-capturing techniques for flows with moving boundaries and interfaces, in: Proceedings of the ASME Symposium on Fluid-Physics and Heat Transfer for Macro- and Micro-Scale Gas-Liquid and Phase-Change Flows (CD-ROM), ASME Paper IMECE2001/HTD-24206, ASME, New York, New York, 2001.

[59] T. E. Tezduyar, Stabilized finite element formulations and interface-tracking and interface-capturing techniques for incompressible flows, in: M. M. Hafez (Ed.), Numerical Simulations of Incompressible Flows, World Scientific, New Jersey, 2003, pp. 221–239.

[60] K. Stein, T. E. Tezduyar, R. Benney, Automatic mesh update with the solid-extension mesh moving technique, Computer Methods in Applied Mechanics and Engineering 193 (21-22) (2004) 2019–2032. doi:10.1016/j.cma.2003.12.046.

[61] Svend Ole Hansen APS, The Hardanger bridge: static and dynamic wind tunnel tests with a section model. Technical report, prepared for Norwegian Public Roads Administration, Tech. rep. (2006).

[62] S. de Miranda, L. Patruno, F. Ubertini, G. Vairo, On the identification of flutter derivatives of bridge decks via RANS turbulence models: Benchmarking on rectangular prisms, Engineering Structures 76 (2014) 359–370. doi:10.1016/j.engstruct.2014.07.027.

[63] L. Patruno, Accuracy of numerically evaluated flutter derivatives of bridge deck sections using RANS: Effects on the flutter onset velocity, Engineering Structures 89 (2015) 49–65. doi:10.1016/j.engstruct.2015.01.034.

[64] M. W. Sarwar, T. Ishihara, K. Shimada, Y. Yamasaki, T. Ikeda, Prediction of aerodynamic characteristics of a box girder bridge section using the LES turbulence model, Journal of Wind Engineering and Industrial Aerodynamics 96 (10-11) (2008) 1895–1911. doi:10.1016/j.jweia.2008.02.015.

[65] K. Takizawa, Y. Bazilevs, T. E. Tezduyar, M.-C. Hsu, O. Øiseth, K. M. Mathisen, N. Kostov, S. McIntyre, Engineering Analysis and Design with ALE-VMS and Space-Time Methods, Archives of Computational Methods in Engineering 21 (4) (2014) 481–508. doi:10.1007/s11831-014-9113-0.

[66] Y. Bai, D. Sun, J. Lin, Three dimensional numerical simulations of long-span bridge aerodynamics, using block-iterative coupling and DES,

Computers and Fluids 39 (9) (2010) 1549–1561. doi:10.1016/j.compfluid.2010.05.005.

[67] A. Šarkić, R. Fisch, R. Höffer, K. U. Bletzinger, Bridge flutter derivatives based on computed, validated pressure fields, Journal of Wind Engineering and Industrial Aerodynamics 104-106 (2012) 141–151. doi:10.1016/j.jweia.2012.02.033.

[68] F. Brusiani, S. D. Miranda, L. Patruno, F. Ubertini, P. Vaona, On the evaluation of bridge deck flutter derivatives using RANS turbulence models, Journal of Wind Engineering 119 (2013) 39–47.

[69] Y. Bai, K. Yang, D. Sun, Y. Zhang, D. Kennedy, F. Williams, X. Gao, Numerical aerodynamic analysis of bluff bodies at a high Reynolds number with three-dimensional CFD modeling, Science China: Physics, Mechanics and Astronomy 56 (2) (2013) 277–289. doi:10.1007/s11433-012-4982-4.

[70] A. Larsen, J. H. Walther, Discrete vortex simulation of flow around five generic bridge deck sections, Journal of Wind Engineering and Industrial Aerodynamics 77-78 (1998) 591–602. doi:10.1016/S0167-6105(98)00175-5.

[71] B. Siedziako, O. Øiseth, A. Rønnquist, An enhanced forced vibration rig for wind tunnel testing of bridge deck section models in arbitrary motion, Journal of Wind Engineering and Industrial Aerodynamics 164 (February) (2017) 152–163. doi:10.1016/j.jweia.2017.02.011.

[72] A. N. Brooks, T. J. R. Hughes, Streamline upwind/Petrov-Galerkin formulations for convection dominated flows with particular emphasis on the incompressible Navier-Stokes equations, Computer Methods in Applied Mechanics and Engineering 32 (1982) 199–259.

[73] T. J. R. Hughes, T. E. Tezduyar, Finite element methods for first-order hyperbolic systems with particular emphasis on the compressible Euler equations, Computer Methods in Applied Mechanics and Engineering 45 (1984) 217–284. doi:10.1016/0045-7825(84)90157-9.

[74] T. E. Tezduyar, Y. J. Park, Discontinuity capturing finite element formulations for nonlinear convection-diffusion-reaction equations, Computer Methods in Applied Mechanics and Engineering 59 (1986) 307–325. doi:10.1016/0045-7825(86)90003-4.

[75] T. J. R. Hughes, L. P. Franca, M. Balestra, A new finite element formulation for computational fluid dynamics: V. Circumventing the Babuška–Brezzi condition: A stable Petrov–Galerkin formulation of the Stokes problem accommodating equal-order interpolations, Computer Methods in Applied Mechanics and Engineering 59 (1986) 85–99.

[76] T. E. Tezduyar, Y. Osawa, Finite element stabilization parameters computed from element matrices and vectors, Computer Methods in Applied Mechanics and Engineering 190 (2000) 411–430. doi:10.1016/S0045-7825(00)00211-5.

[77] T. E. Tezduyar, Computation of moving boundaries and interfaces and sta-

bilization parameters, International Journal for Numerical Methods in Fluids 43 (2003) 555–575. doi:10.1002/fld.505.

[78] T. J. R. Hughes, G. Scovazzi, L. P. Franca, Multiscale and stabilized methods, in: E. Stein, R. de Borst, T. J. R. Hughes (Eds.), Encyclopedia of Computational Mechanics, Vol. 3, Fluids, Wiley, 2004, Ch. 2.

[79] T. E. Tezduyar, S. Sathe, Modeling of fluid–structure interactions with the space–time finite elements: Solution techniques, International Journal for Numerical Methods in Fluids 54 (2007) 855–900. doi:10.1002/fld.1430.

[80] Y. Bazilevs, V. M. Calo, T. J. R. Hughes, Y. Zhang, Isogeometric fluid–structure interaction: theory, algorithms, and computations, Computational Mechanics 43 (2008) 3–37.

[81] M.-C. Hsu, Y. Bazilevs, V. M. Calo, T. E. Tezduyar, T. J. R. Hughes, Improving stability of stabilized and multiscale formulations in flow simulations at small time steps, Computer Methods in Applied Mechanics and Engineering 199 (2010) 828–840.

[82] K. Takizawa, T. E. Tezduyar, Multiscale space–time fluid–structure interaction techniques, Computational Mechanics 48 (2011) 247–267. doi:10.1007/s00466-011-0571-z.

[83] K. Takizawa, T. E. Tezduyar, Space-Time Fluid-Structure Interaction Methods, Mathematical Models and Methods in Applied Sciences 22 (supp02) (2012) 1230001. doi:10.1142/S0218202512300013.

[84] J. Chung, G. M. Hulbert, A Time Integration Algorithm for Structural Dynamics With Improved Numerical Dissipation: The Generalized-α Method, Journal of Applied Mechanics 60 (2) (1993) 371–375. doi:10.1115/1.2900803.

[85] K. E. Jansen, C. H. Whiting, G. M. Hulbert, A generalized-α method for integrating the filtered Navier-Stokes equations with a stabilized finite element method, Comput. Methods Appl. Mech. Engrg. 190 (2000) 305–319.

[86] G. Parkinson, N. Brooks, On the aeroelastic instability of bluff cylinders, Journal of applied mechanics 47 (1961) 557–566.

[87] Y. Tamura, A. Kareem, Advanced structural wind engineering, Springer Japan, Vol. I, 2013.

[88] T. Theodorsen, General theory of aerodynamic instability and the mechanism of flutter (1935).

[89] R. H. Scanlan, J. Tomko, Airfoil and bridge deck flutter derivatives, Journal of the Engineering Mechanics Division 97 (6) (1971) 1717–1737.

[90] A. Jain, N. P. Jones, R. H. Scanlan, Coupled Flutter and Buffeting Analysis of Long-Span Bridges, Journal of Structural Engineering 122 (7) (1996) 716–725. doi:10.1061/(ASCE)0733-9445(1996)122:7(716).

[91] L. Singh, N. P. Jones, R. H. Scanlan, O. Lorendeaux, Identification of lateral flutter derivatives of bridge decks, Journal of Wind Engineering and Industrial Aerodynamics 60 (1-3) (1996) 81–89. doi:10.1016/0167-6105(96)00025-6.

[92] R. H. Scanlan, A. Sabzevari, Experimental Aerodynamic Coefficients in the Analytical Study of Suspension Bridge Flutter, Journal of Mechanical Engineering Science 11 (3) (1969) 234–242. doi:10.1243/JMES_JOUR_1969_011_031_02.

[93] R. L. Halfman, Experimental Aerodynamic Derivatives of a Sinusoidally Oscillating Airfoil in Two-Dimensional Flow, Tech. rep., Massachusetts Inst. of Tech.; Cambridge. (1952).

[94] F. L. Haan, A. Kareem, A. A. Szewczyk, The effects of turbulence on the pressure distribution around a rectangular prism, Journal of Wind Engineering and Industrial Aerodynamics 77 (1998) 381–392. doi:10.1016/S0167-6105(98)00158-5.

[95] R. R. Sarkar, N. P. Jones, R. H. Scanlan, Identification of aeroelastic parameters of flexible bridges., ASCE J. Eng. Mech. 120 (8) (1994) 1718–1742.

[96] P. P. Sarkar, L. Caracoglia, F. L. Haan, H. Sato, J. Murakoshi, Comparative and sensitivity study of flutter derivatives of selected bridge deck sections, Part 1: Analysis of inter-laboratory experimental data, Engineering Structures 31 (1) (2009) 158–169. doi:10.1016/j.engstruct.2008.07.020.

[97] A. Zanotti, R. Nilifard, G. Gibertini, A. Guardone, G. Quaranta, Assessment of 2D / 3D numerical modeling for deep dynamic stall experiments, Journal of Fluids and Structures 51 (2014) 1–19. doi:10.1016/j.jfluidstructs.2014.08.004.

[98] A. K. Karanam, K. E. Jansen, C. H. Whiting, Geometry based pre-processor for parallel fluid dynamic simulations using a hierarchical basis, Engineering with Computers 24 (1) (2007) 17–26. doi:10.1007/s00366-007-0063-0.

[99] M.-C. Hsu, I. Akkerman, Y. Bazilevs, High-performance computing of wind turbine aerodynamics using isogeometric analysis, Computers and Fluids 49 (1) (2011) 93–100. doi:10.1016/j.compfluid.2011.05.002.

[100] G. Bianchi, Electronic Filter Simulation & Design, McGraw Hill Professional, 2007.

[101] T. A. Helgedagsrud, K. M. Mathisen, Y. Bazilevs, O. Øiseth, A. Korobenko, Using ALE-VMS to compute wind forces on moving bridge decks, in: B. Skallerud, H. I. Andersson (Eds.), Proceedings of MekIT'17 Ninth National Conference on Computational Mechanics, CMIME, Barcelona, Spain, 2017, pp. 169–189.

[102] O. Øiseth, A. Rönnquist, R. Sigbjörnsson, Simplified prediction of wind-induced response and stability limit of slender long-span suspension bridges, based on modified quasi-steady theory: A case study, Journal of Wind Engineering and Industrial Aerodynamics 98 (12) (2010) 730–741. doi:10.1016/j.jweia.2010.06.009.